Double Modulation and Microstructure of the Thermoelectric Misfit Compound $[Ca_{2-y}Ln_yCu_{0.7+y}Co_{1.3-y}O_4][CoO_2]_{b_1/b_2}$ (Ln = Pr, Y and $0 \leq y \leq 1/3$)

N. Créon, O. Perez,* J. Hadermann,† Y. Klein, S. Hébert, M. Hervieu, and B. Raveau

Laboratoire CRISMAT, ENSICAEN, 6 bd Maréchal Juin,14050 Caen, Cedex 4 France

Received May 17, 2006. Revised Manuscript Received July 25, 2006

In the present paper, we present one route for increasing the copper content in the misfit cobaltites by studying the $[Ca_{2-y}Ln_yCu_{0.7+y}Co_{1.3-y}O_4][CoO_2]_{b_1/b_2}$ (Ln = Pr,Y) series (Ln = magnetic Pr and nonmagnetic Y). We pay special attention to the modulated character of these compounds. The electron diffraction study shows a double modulation of the structure. The parameters of the two systems (rock salt and CdI_2 types) are $a_1 = a_2 = 4.805(9)$ Å, $b_1 = 4.482(9)$ Å, $b_2 = 2.804(9)$ Å, $c_1 = c_2 = 12.75(3)$ Å, and $\beta_1 = \beta_2 = 93.7(2)°$, $\nu = b_1/b_2 = 1.599(4)$. The first modulation vector $\mathbf{q}_1^* = 0.63b_1^*$ is associated with the misfit character of the compound, and the second one, $\mathbf{q}_2^* = 0.44a_1^* + 0.43c_1^*$, is an intrinsic modulation of the rock salt layers. Accounting for this second modulation, the reconstruction of the reciprocal space leads the super-space group $C2/m(1q0,\alpha 0\gamma)mm$, with $\mathbf{q}_1^* = 0.63b_1^*$ and $\mathbf{q}_2^* = 0.44a^* + 0.43c^*$. The intrinsic modulation in the double $[(Co,Cu)O]_2$ rock salt-type layer of a misfit cobaltite is shown for the first time by electron microscopy. Different twinning mechanisms are also characterized. The relationships with the strontium ferrites built up from four rock salt-related layers are discussed. An increase of the thermopower is obtained, as well with a magnetic (Pr) as a nonmagnetic (Y) cation, which shows that the enhancement is due to a valence effect rather than to a magnetic effect.

Introduction

The discovery of large thermoelectric power in Na_xCoO_2[1] had renewed, a few years ago, interest in layered cobaltites. The A_xCoO_2 structures are built up from one hexagonal $[CoO_2]_\infty$ layer alternating with one $[A_x]_\infty$ layer, x varying in a large homogeneity range and depending on the nature of A.[1−4] Similar hexagonal $[TS_2]_\infty$ layers are observed in the chalcogenide structures,[5] sandwiching one rock salt-type slice made of two adjacent $[MS]_\infty$ sheets. The difference in symmetry of the two types of layers implying the formation of the so-called "misfit layer compounds". This structural mechanism was extended by the discovery of cobaltites with original misfit layered structures.[6−11] These composite structures are described considering two sub-lattices. Double or triple rock salt-type blocks, built up of three or four $[AO]_\infty$ sheets, respectively, form the first sub-lattice and are stacked up with $[CoO_2]_\infty$ layers, which form the second sub-lattice. The two subsystems exhibit the same periodicity along a and c whereas the composite character of the structure appears with two different parameters b_1 (first sub-lattice) and b_2 (second sub-lattice) along b. As a consequence of this misfit, a modulation is observed between the two sub-lattices, and the b_1/b_2 ratio varies with composition between 1.62 for $Ca_3Co_4O_9$[7] and 2.0 for $[Bi_2Ba_{1.8}Co_{0.2}O_4][CoO_2]_2$,[12] the first one being characterized by three $[AO]_\infty$ sheets (**3S**) and the second by four $[AO]_\infty$ sheets (**4S**) (Figure 1). The chemical formulation is usually noted as follows: [first sub-lattice][second sub-lattice]$_{b_1/b_2}$.

The appearance of a second modulation first reported in the (**4S**) cobaltite, $[Bi_{1.74}Sr_2O_4][CoO_2]_{1.82}$,[11] increases considerably the structural complexity. Leligny et al.[11] have described this modulation along a and c as an intrinsic modulation in the rock salt-type layer associated to the presence of double bismuth layer in the stacking sequence $[SrO]_\infty[BiO]_\infty[BiO]_\infty[SrO]_\infty$ along the c axis (Figure 1). This intrinsic modulation vector of $[Bi_{1.74}Sr_2O_4][CoO_2]_{1.82}$ is $\mathbf{q}^* = 0.293a^* + 0.915c^*$. Such a modulation phenomenon is common to the large families of cuprates (see ref 13 for

* Corresponding author. E-mail: olivier.perez@ensicaen.fr.
† Present address: EMAT, University of Antwerpen, Groenenborgerlaan, Antwerpen, Belgium.

(1) Terasaki, I.; Sasago, Y.; Uchinokura, K. *Phys. Rev. B* **1997**, *56*, 12685.
(2) Johnston, W. D.; Heikes, R. R.; Sestrich, D. *J. Phys. Chem. Solids* **1958**, *7*, 1−13.
(3) Douakha, N.; Holzapfel, M.; Chappel, E.; Chouteau, G.; Croguennec, L.; Ott, A.; Ouladdiaf, B. *J. Solid State Chem.* **2002**, *163*, 406−411.
(4) Jansen, M.; Hoppe, R. *Z. Anorg. Allg. Chem.* **1974**, *408*, 97−103.
(5) Wiegers, G. A.; Meerschaut, A. *J. Alloys Compd.* **1992**, *178*, 351.
(6) Boullay, P.; Domengès, B.; Hervieu, M.; Groult, D.; Raveau, B. *Chem. Mater.* **1996**, *8*, 1482−1489.
(7) Masset, A. C.; Michel, C.; Maignan, A.; Hervieu, M.; Toulemonde, O.; Studer, F.; Raveau, B. *Phys. Rev. B* **2000**, *62*, 166.
(8) Lambert, S.; Leligny, H.; Grebille, D. *J. Solid State Chem.* **2001**, *160*, 322−331.
(9) Miyazaki, Y.; Miura, T.; Ono, Y.; Kajitani, T. *Jpn. J. Appl. Phys.* **2002**, *41*, L849−L851.
(10) Pelloquin, D.; Maignan, A.; Hebert, S.; Martin, C.; Hervieu, M.; Michel, C.; Wang, L.-B.; Raveau, B. *Chem. Mater.* **2002**, *14*, 3100−3105.
(11) Leligny, H.; Grebille, D.; Pérez, O.; Masset, A. C.; Hervieu, M.; Raveau, B. *Acta Crystallogr. B* **2000**, *56*, 173−182.
(12) Hervieu, M.; Maignan, A.; Michel, C.; Hardy, V.; Créon, N.; Raveau, B. *Phys. Rev. B* **2003**, *67*, 045112.
(13) Raveau, B.; Michel, C.; Hervieu, M.; Groult, D. *Crystal Chemistry of High Tc Superconducting Copper Oxides*; Springer Series in Materials Science 15; Springer-Verlag: New York, 1991; 331 pp.

10.1021/cm061163a CCC: $33.50
Published on Web 10/10/2006

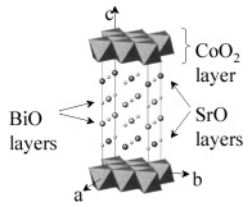

Figure 1. Schematical drawing of the (**4S**) structure of the $[Bi_{1.74}Sr_2O_4]$-$[CoO_2]_{1,82}$ cobaltite.[11]

review), cobaltites,[14,15] and ferrites.[16−20] In these 2201's, 2212's, and 2223's (using the nomenclature adopted for the superconducting cuprates[13]), the two intermediate sheets contain large d^{10} metals (i.e., Bi, Tl, and/or Hg). Miyazaki et al. have recently presented another layered (**4S**) cobaltite, $[Ca_2(Co_{0.65}Cu_{0.35})_2O_4][CoO_2]_{1.60}$,[9,21] which exhibits the distinctive feature to present two intermediate sheets containing transition metal, sandwiched in between the two $[CaO]_\infty$ sheets. Such a double $[AO]_\infty$ sheet of transition metal sandwiched between two $[SrO]_\infty$ sheets to form a modulated block directly related to the rock salt-type structure is also observed in $Sr_4Fe_6O_{13}$[23,24] and $Bi_4Sr_{14}Fe_{24}O_{56}$[25] ferrites.

In the present paper, we have investigated one route for increasing the copper content and studied the nanostructure of the $[Ca_{2-y}Ln_yCu_{0.7+y}Co_{1.3-y}O_4][CoO_2]_{b_1/b_2}$ (Ln = Pr,Y) misfit cobaltites (Ln = magnetic Pr and nonmagnetic Y), paying special attention to the modulated character and the twinning phenomena associated with the distortion of the two sub-lattices through their connection.

Experimental Section

The samples have been prepared by intimate mixing of stoichiometric amounts of the rare earth component (Pr_6O_{11}, Tb_2O_3, Tb_2O_3, Yb_2O_3, or Lu_2O_3) with CaO, CuO, and Co_3O_4 powders. The intimate mixtures were pressed in the form of bars and heated in alumina crucibles under oxygen at 915 °C for 24 h. This procedure was repeated four times, after intermediate grinding, to eliminate the impurity phase $Ca_3Co_4O_9$, which is formed during the early stages of the reaction. The purity and homogeneity of the samples were checked using energy dispersive spectroscopy (EDS), X-ray powder, and electron diffraction techniques.

The X-ray powder diffraction (XRDP) data were collected at room temperature in the range of $10° \leq 2\theta \leq 90°$ by increment of 0.02° with a Philips X'PERT PRO diffractometer working with the Cu Kα radiation. The sample was sprinkled onto a greased single crystal of silicium with a rotating sample holder with the aim of limiting background and preferential orientation.

Neutron diffraction experiment was carried out at the Léon Brillouin Laboratory (CEA, Saclay, France) with the high-resolution 3T2 diffractometer using a Ge(335) monochromator and a wavelength of $\lambda = 1.2251$ Å at room temperature. The 2θ range was from 6 to 125° in steps of 0.05°. Data were analyzed by the Rietveld method using JANA programs.[26]

Samples for transmission electron microscopy (TEM) were prepared by crushing the bars in ethanol and depositing the small crystallites onto a holey carbon film, supported by a nickel grid. The electron diffraction (ED) and high-resolution electron microscopy (HREM) were carried out at room temperature with JEOL 200 CX, JEOL2011, and TOPCON 002B electron microscopes equipped with EDS analyzers.

Thermogravimetric analyses were performed with a TAG 92 Setaram. Oxidation rate was measured by heating samples under Ar/H_2 (X %) flow up to 900 °C at 5 °C·min^{-1}. Stability of the samples was tested under air and oxygen flow heating up to 1100 °C at 2.5 °C·min^{-1}.

Electrical indium contacts were ultrasonically deposited on bars with typical dimensions of $2 \times 2 \times 10$ mm^3 to perform resistance (four-probe technique) and thermoelectric power (steady-state method) measurements. These data sets were obtained using a Quantum Design Physical Properties measurements system (PPMS).

Results

A first investigation of the diagram Ca−Cu−Co−O was carried out for determining the key factors governing the formation of the (**4S**) misfit phase. It showed that its stabilization is strongly dependent on the oxygen pressure, systematically leading to the formation of the highly stable misfit cobaltite (**3S**) $Ca_3Co_4O_9$.[7] Following the above-mentioned synthesis process, the combined EDS and thermogravimetric analyses of the $y = 0$ sample led to the composition $[Ca_2Cu_{0.7}Co_{1.3}O_4][CoO_2]_{1.59}$ (in the limits of accuracy of the techniques), which implies an average valence of +3.5 for cobalt on the basis of divalent copper. We have therefore selected a double substitution route through the nominal formulation $[Ca_{2-y}Ln_yCu_{0.7+y}Co_{1.3-y}O_4][CoO_2]_{b_1/b_2}$, selecting first Pr^{3+} for its ionic radius close to that of Ca^{2+}, expecting that the b_1/b_2 ratio, which was determined as one of the key factors in the alkaline earth bismuth cobaltites,[11−12] remains roughly constant. Y^{3+} was then selected due to its nonmagnetic character.

X-ray diffraction (Figure 2a) showed that single-phased samples are formed for $0 \leq y \leq 0.27$ for Ln = Pr and up to 0.33 for Ln = Y. As described in the next section, the parameters have been refined from X-ray diffraction patterns using the super-space formalism and the two sub-lattices: $a \approx 4.8$ Å, $b_1 \approx 4.5$ Å, $c \approx 12.7$ Å, $b_2 \approx 2.8$ Å, $\beta \approx 93.9°$. The $[Ca_{2-y}Pr_yCu_{0.7+y}Co_{1.3-y}O_4][CoO_2]_{b_1/b_2}$ cell parameters as a function of y are given in Table 1. One observes a slight and regular increase of the b_1 and c parameters as the praseodymium content as x increases, whereas a, b_2, and β

(14) Leligny, H.; Durcok, S.; Labbe, P.; Ledesert, M.; Raveau, B. *Acta Crystallogr. B* **1992**, *48*, 407−418.
(15) Jakubowicz, N.; Grebille, D.; Leligny, H.; Evain, M. *J. Phys. Condens. Matter* **1999**, *11*, 3997.
(16) Lepage, Y.; Mc Kinnon, W. R.; Tarascon, J. M.; Barboux, P. *Phys. Rev. B* **1989**, *40*, 6810.
(17) Hervieu, M.; Michel, C.; Nguyen, N.; Retoux, R.; Raveau, B. *Eur. J. Solid State Chem.* **1988**, *25*, 375.
(18) Retoux, R.; Michel, C.; Hervieu, M.; Nguyen, N.; Raveau, B. *Solid State Commun.* **1989**, *69*, 599.
(19) Pissas, M.; Papaefthymiou, V.; Simopoulos, A.; Kostikas, A.; Niarchos, D. *Solid State Commun.* **1990**, *73*, 767.
(20) Hervieu, M.; Pelloquin, D.; Michel, C.; Caldes, M. T.; Raveau, B. *J. Solid State Chem.* **1995**, *118*, 227.
(21) Miyazaki, Y.; Miura, T.; Onoda, M.; Uchida, M.; Ishii, Y.; Ono, Y.; Morii, Y.; Kajitani, T. *Jpn. J. Appl. Phys.* **2003**, *42*, 7467−7473.
(22) Rossell, M. D.; Abakumov, A. M.; Van Tendeloo, G.; Pardo, J. A.; Santiso, J. *Chem. Mater.* **2004**, *16*, 2578.
(23) Hervieu, M.; Pelloquin, D.; Michel, C.; Caldés, M. T.; Raveau, B. *J. Solid State Chem.* **1995**, *118*, 227.
(24) Mellenne, B.; Retoux, R.; Lepoittevin, C.; Hervieu, M.; Raveau, B. *Chem. Mater.* **2004**, *16*, 5006−5013.
(25) Rossell, M. D.; Abakumov, A. M.; Van Tendeloo, G.; Pardo, J. A.; Santiso, J. *Chem. Mater.* **2004**, *16*, 2578.
(26) Lepoittevin, C.; Malo, S.; Hervieu, M.; Grebille, D.; Raveau, B.; Rodriguez-Carvajal, J. *FULLPROF*, version May 2001; LLB-CEA: Saclay, France, 2001.

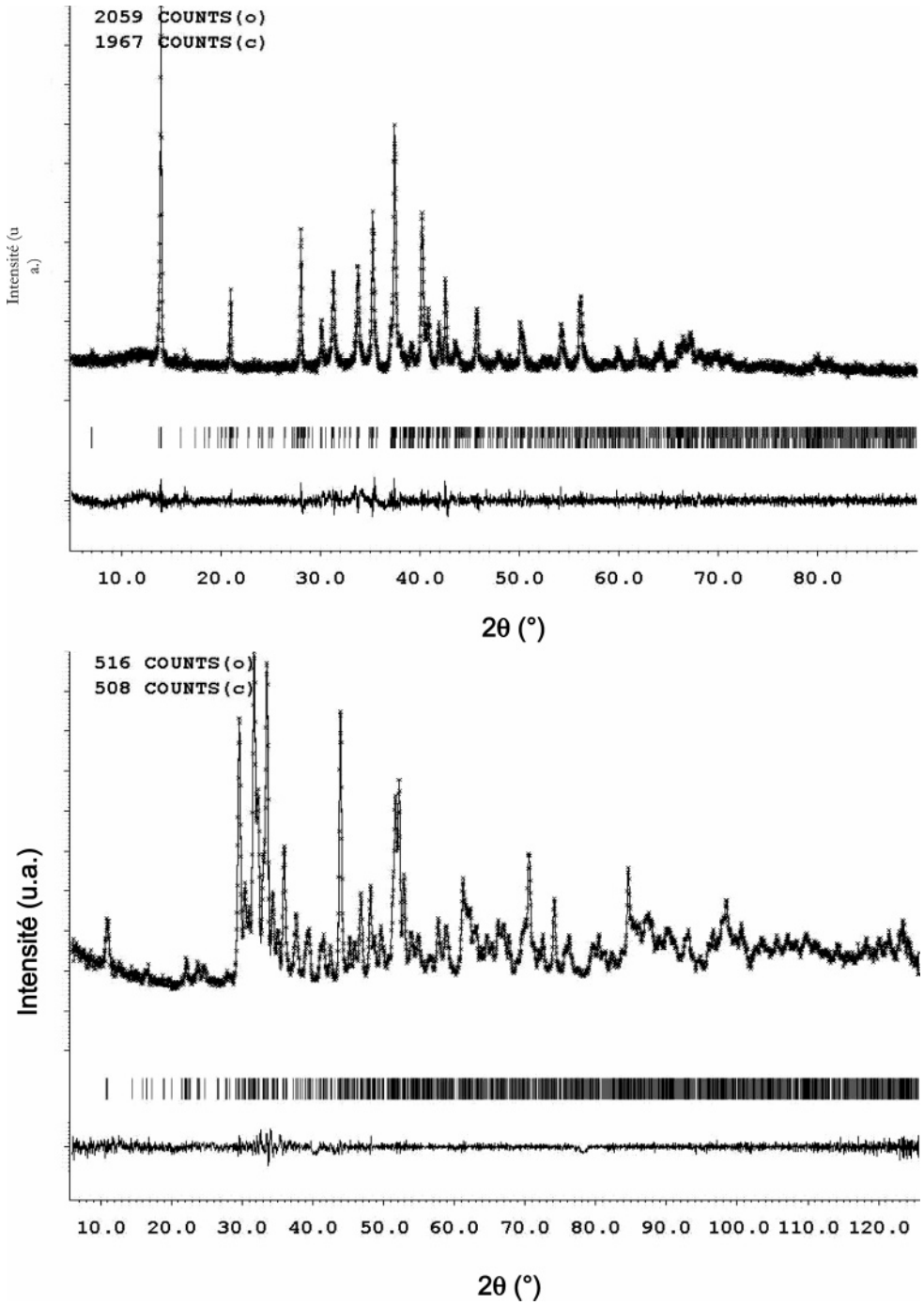

Figure 2. (a) XRD and (b) ND patterns of $[Ca_2(Co_{1.3}Cu_{0.7})][CoO_2]_{1.59}$. Observed, calculated, and the difference are plotted on the same scale.

Table 1. Cell Parameters of $[Ca_{2-y}Ln_yCu_{0.7+y}Co_{1.3-y}O_4][CoO_2]_{b_1/b_2}$

y	detailed formula	a (Å)	b_1 (Å)	c (Å)	b_2 (Å)	β (°)	b_1/b_2
0	$[Ca_2(Co_{1.3}Cu_{0.7})\ O_4][CoO_2]_{1.59}$	4.817(2)	4.482(2)	12.765(6)	2.804(3)	93.61(1)	1.594
0.07	$[Ca_{1.93}Pr_{0.07}(Co_{1.23}Cu_{0.77})\ O_4][CoO_2]_{1.60}$	4.817(2)	4.489(2)	12.778(4)	2.812(2)	93.95(2)	1.596
0.13	$[Ca_{1.87}Pr_{0.13}(Co_{1.17}Cu_{0.83})\ O_4][CoO_2]_{1.60}$	4.817(2)	4.504(2)	12.784(5)	2.819(3)	93.88(3)	1.598
0.20	$[Ca_{1.80}Pr_{0.20}(Co_{1.10}Cu_{0.90})\ O_4][CoO_2]_{1.60}$	4.818(3)	4.509(3)	12.781(9)	2.815(4)	93.97(4)	1.602
0.27	$[Ca_{1.73}Pr_{0.27}(Co_{1.03}Cu_{0.97}\ O_4)]\ [CoO_2]_{1.60}$	4.819(2)	4.520(2)	12.782(6)	2.815(3)	93.93(3)	1.606

parameters remain constant. The latter parameters are characteristic of the "hexagonal" $[CoO_2]$ layers, showing that their distortion does not evolve with the Pr and Cu introduction. Since Ca^{2+} and Pr^{3+} have similar ionic radius, [r_{Ix} = 1.18 Å], the increase of the b_1 and c parameters could be rather associated to the presence of copper and its Jahn−Teller effect in the medium layer of the rock salt system.

In the case of the Y phase, no significant evolution of the different parameters and b_1/b_2 ratio have been detected with regard to the pure calcium phase, up to the limit compound $[Ca_{1.67}Y_{0.33}Cu_{1.03}Co_{0.97}O_4][CoO_2]_{1.59}$. This effect can be generated by the smaller radius of Y ($r(Y_{Ix}^{3+})$ = 1,07 Å), which could compensate for the Cu effect. It is interesting to note that, in both systems, the limit of the existence range

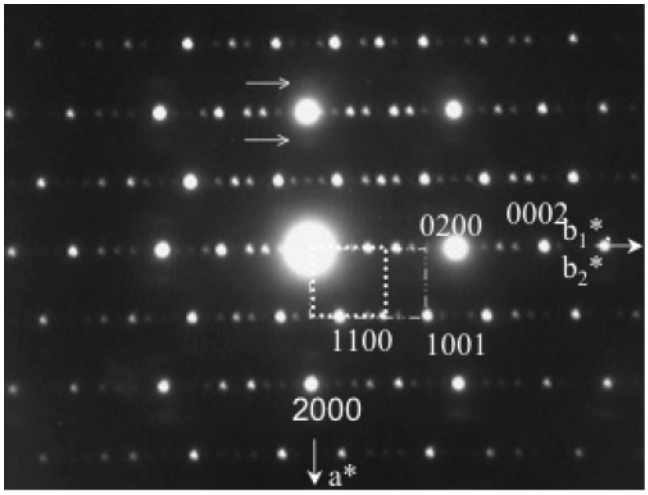

Figure 3. [0010] ED patterns: the two sub-lattices, with common *a** axes and different but parallel b_1* and b_2* axes, are drawn with dotted lines.

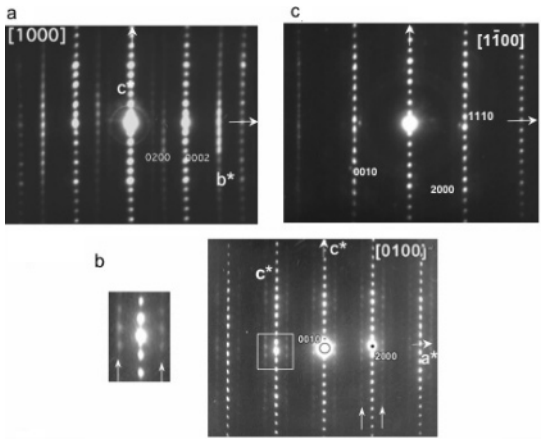

Figure 4. Typical (a) [0100], (b) [1000] and enlarged satellites and $\bar{2}000$ reflection, (c) [1100] ED patterns.

corresponds to a ratio Co/Cu ≈ 1 in the two internal layers of the rock salt system.

Electron Diffraction. The transmission electron microscopy study shows a strong preferential orientation of the crystallites, whatever *y*, mainly along [0010] as previously reported for other misfit cobaltites.

The reconstruction of the reciprocal space confirmed the misfit character of the samples and the presence of two sub-lattices, both monoclinic and C-centered. The sub-lattices have the same periodicity along *a* and *c* but have different *b* parameters. These parameters are $a \approx 4.82$ Å, $b_1 \approx 4.49$ Å, $c \approx 12.66$ Å, $b_2 \approx 2.81$ Å, $\beta = 93.9°$. Typical electron diffraction patterns are given in Figures 3 and 4. The ED patterns are indexed considering the main reflections of the second subsystem as satellite reflections of the *M*th order of the *h*0l reflections of the first subsystem, as is common practice with misfit cobaltites. The diffraction vector can then be written as $\mathbf{s}^* = ha_1^* + kb_1^* + lc_1^* + Mq^*$ with $\mathbf{q}^* = a_2^* + b_2^* = a_1^* + b_2^*$ as the modulation vector to the first subsystem. This can be also rewritten as $\mathbf{s}^* = Ha_1^* + Kb_1^* + Lc_1^* + Mb_2^*$ with $H = h + M$, $K = k$, $L = l$. This means that the reflections *HKL*0 are the main reflections of the first sub-lattice, *H*0*LM* are the main reflections of the second sub-lattice. *HKLM* are the satellite reflections due to both subsystems. The condition *hkl*: $h + k = 2n$, related to the *C* lattice, leads to the condition *HKLM*: $H + K + M = 2n$, involving a (1/2, 1/2, 0 1/2) centering in the 4D space. All observed reflections are in agreement with this general condition, except 0*K*0*M*: $M = 2n$, which is stricter than the 0*K*0*M*: $K + M = 2n$ (deduced from the general condition). These reflection conditions are in agreement with a space group $C2/m(1q0)s0$, the modulation vector being $\mathbf{q}_1^* = 0.63b_1^*$. The two sub-cells are drawn in dotted lines in the [0010] ED pattern given in Figure 3.

The important point of this ED study deals with the evidence of a second modulation characterized by a vector $\mathbf{q}_2^* = 0.44a^* + 0.43c^*$. In order to simplify the description of the ED pattern orientations, we keep the indices of the first subsystem zone axes. The extra reflections are clearly observed, as indicated by the white arrows in the [0100] ED pattern and its enlarged white-framed part (Figure 4b). In the [0010] ED patterns, their signatures only consist in weak and streaky satellites (see the two white arrows in the top part of Figure 3). Accounting for the second modulation, the reconstruction of the reciprocal space showed that the space group becomes $C2/m(1q0,\alpha0\gamma)mm$, with $\mathbf{q}_1^* = 0.63b_1^*$ and $\mathbf{q}_2^* = 0.44a^* + 0.43c^*$. This second modulation is associated to an intrinsic modulation in the rock salt-type layer because each extra spot is linked to an *HK*00 spot. Intrinsic modulations of the rock salt slabs were already reported in the misfit compounds $[Bi_{1.74}Sr_2O_4][CoO_2]_{1,82}$,[11] ($\mathbf{q}_2^* = 0.293a^* + 0.915c^*$)[11] and $[Bi_2Ba_{1.8}Co_{0.2}O_4][CoO_2]_2$ ($\mathbf{q}_2^* = 0.2a^* + 0.2b^*$).[12]

Note that despite the modulation vector is $\mathbf{q}_2^* = 0.44a^* + 0.43c^*$, diffuse satellites associated with the intrinsic modulation are observed viewing the crystals along [0010] (white arrows Figure 3a), due to their plate-like shape. As previously reported for these misfit cobaltites, numerous crystallites are twinned in correlation with the monoclinic distortion of the sub-lattices, each of them generating their own variants.

Structure Refinement. The ED results evidencing the great similarities of the samples as a function of *y*, the ternary compound $[Ca_2(Co_{1.3}Cu_{0.7})O_4][CoO_2]_{1.59}$ ($y = 0$) was selected for the powder diffraction study. The data were studied using the Jana2000 program[27] and the super-space formalism developed for modulated structure.[28] Pattern matching analysis, calculated for main and first-order satellite reflections, confirms the cell parameters observed by electron diffraction. The agreement factors are $R_p = 0.023$, $R_{wp} = 0.031$ for five cell parameters, one global shift parameter, three profile parameters, and six background parameters. The neutron diffraction pattern can be indexed using two subsystems with the following cell parameters: $a_1 = a_2 = 4.805(9)$ Å, $b_1 = 4.482(9)$ Å, $b_2 = 2.804(9)$ Å, $c_1 = c_2 = 12.75(3)$ Å, and $\beta_1 = \beta_2 = 93.7(2)°$, $\nu = b_1/b_2 = 1.599(4)$. In agreement with ED observations, the $C2/m(1\nu0)s0$ super-space group was chosen.

The structure was then refined using a starting model, which has been defined using HREM observations; powder diffraction data were analyzed by Rietveld method. Subsystem 1 (i.e., $Ca_2(Co,Cu)_2O_4$) was considered as a reference. The diffraction pattern (Figure 2b) is very complex, and it was impossible to discriminate the contribution of back-

Table 2. Atomic Positions

atom	*x*	*y*	*z*	U_{iso} (Å^2)
Subsystem 1: $Ca_2(Co,Cu)_2O_4$				
Ca(1)	0.508(14)	0[a]	0.265(5)	0.01[b]
Co(1)/Cu(1)	0.048(16)	0[a]	0.419(5)	0.01[b]
O(1)	0.492(11)	0[a]	0.390(3)	0.01[b]
O(2)	−0.072(12)	0[a]	0.286(4)	0.01[b]
Subsystem 2: CoO_2				
Co(2)	0.75[a]	0.75[a]	0[a]	0.01[b]
O(3)	0.905(11)	0.25[a]	−0.119(3)	0.01[b]

[a] Fixed by symmetry. [b] Fixed during the refinement.

ground, main and first-order satellite reflections. Therefore, displacement modulation functions were not introduced during our refinements, ca. the interaction between the two subsystems was not taking into account. This induces some anomalies in our model, as too short Ca−O distances (≈2 Å). Atomic displacement parameters were then fixed to U_{iso} = 0.01 Å. Final refined structural parameters are given in Table 2 (final reliability factors: $R_{obs} = 0.132$, $R_{wobs} = 0.138$, $R_p = 0.11$, $R_{wp} = 0.147$, and $\chi^2 = 2.9$). Figure 5 shows the resulting model projected along *a*.

High-Resolution Electron Microscopy. The [1100] direction allows easily the stacking mode of the rock salt layers along the *c* axis to be imaged, as previously shown for the complex superconducting cuprates and other misfit cobaltites. A typical [1100] HREM image is given in Figure 6, where the bright dots are associated to the cation positions: the four rows of staggered bright spots parallel to [1$\bar{1}$00] confirm the presence of four $[AO]_\infty$ sheets forming the triple rock salt layers of the (**4S**)-type structure and separated by a single row of coalescent bright dots associated to the $[CoO_2]_\infty$ layer. This image is in agreement with the models proposed for $[Bi_{1.74}Sr_2O_4][CoO_2]_{1.82}$[11] and $[Ca_2(Co_{0.65}Cu_{0.35})_2O_4][CoO_2]_{1.60}$,[21−22] as shown from the good fit with the theoretical images (focus value close to −600 Å). These images have been calculated accounting for an approximate commensurate image with $a = 4.84$ Å, $b' \approx 5b_1 \approx 8b_2 \approx 22.4$ Å, $c = 12.76$ Å, and $\beta = 93°6$, leading to $b_1/b_2 = 1.6$. This theoretical approximant model was made considering each atom is independent so that the simulation was performed in the space group *P*1 due to the incommensurate character of the misfit structure (Figure 6).

Another important piece of information is obtained viewing the crystallites along [0100], as illustrated by the typical image given in Figure 7a. Along that direction, for the same focus value, the four $[AO]_\infty$ sheets appear as four rows of aligned bright dots, separated by small elongated gray dots associated to the $[CoO_2]_\infty$ layers. The overview (Figure 7a) shows clearly a modulation of the contrast along **a** at the level of the four $[AO]_\infty$ sheets, with alternating bright and less bright zones especially visible in the thick parts of the crystallites, on the one hand, and also the variation of the contrast all along a few $[CoO_2]_\infty$ layers (see white arrows), on the other hand. It also shows the existence of planar-like defects, indicated by horizontal white arrows, and the formation of curved layers (vertical arrow).

The enlarged image in Figure 7b shows that the bright and less bright zones are generated by the alternation of two bright sticks separated by two or three gray sticks. The sticks are perpendicular to *a* and generated by the coalescence of the four dots in the thick part of the crystallite. White and dark numbers denote them in the lower part of the image and the present experimental sequence (**3222223222322322322**) leads to an average value of the periodicity 40/18a ≈ 1/0.45, which is in agreement with the modulation vector determined from ED. Such a contrast can be compared to those observed in the Bi based cuprates and the $Sr_4Fe_6O_{13}$[23,24] or $Bi_4Sr_{14}Fe_{24}O_{56}$[25] ferrites. It is associated to a displacive modulation and modulated occupancy of the oxygen atoms located in the two intermediate $[AO]_\infty$ sheets, double $[BiO_{1+\delta}]$, and $[FeO_{1+\delta}]$ layers, respectively. Simulation of the modulated contrast could not be carried out due to the lack of information in the neutron data.

The second structural mechanism observed in the enlarged HREM images is the possible "rotation" of the single hexagonal $[CoO_2]_\infty$ layers around the *c* axis by twinning phenomena, independently of the rock salt blocks. The image calculations were carried out using two layered structure-types, one being the $[AO]_\infty$ sheet and the second the hexagonal $[CoO_2]_\infty$ layer; they are superimposed with the experimental images. Due to the complexity of the intrinsic modulation vector value (**q*** = 0.44*a** + 0.43*c**), the modulation was approximated along these directions to **q*** = 0.5*a** + 0.5*c** (the model is given in Figure 8b). Figure 7b shows that the modulation is established over the whole crystal, so that we have keep unchanged the [0100] orientation of the [AO] sheet, whereas the hexagonal layer suffers rotations of 180° and 120°. The $[AO]_\infty$ sheets appear as four rows of bright dots and the CoO_6 octahedra of the hexagonal layer as tilted and elongated dots. At the level of the defect, it clearly appears that the rock salt block remains unchanged but that the elongated dots are symmetrically tilted along a direction perpendicular to the layers. Since the translation of the rock salt block is not disturbed by this change in direction, the phenomenon can be interpreted as a 180° rotation of one $[CoO_2]_\infty$ layer (Figure 8b). In the second enlarged image (Figure 8c), the contrast at the level of the hexagonal $[CoO_2]_\infty$ layer appears as a quite vertical and elongated dot. The image calculations confirm that it can be interpreted from a 120° orientation of the $[CoO_2]_\infty$ layer. It can be considered as the association of one [0100] modulated $[AO]_\infty$ sheet with a [1100] $[CoO_2]_\infty$ layer, which induces strain effects, originating the planar variation of the contrast indicated by horizontal arrows in Figure 7b. These images illustrate the numerous twinning mechanisms due to the distortion of the two (pseudo-cubic and pseudo-hexagonal) subsystems and all the combined variants. They show how frequent they are, appearing concomitantly in the lamellar crystallites. Note that, when arising at the nanometer scale, such a chemical twinning (Figure 9a) involves the local stabilization of another structural polytype of the compound, which is characterized by a double orthorhombic subcell with $a_1 = a_2 \approx 4.8$ Å, $b_1 = 4.48$ Å, $b_2 = 2.80$ Å, $c_0 = 2c_1 = 2c_2 \approx 25.5$ Å, and $\beta_0 = 90$ (the orientation of the two twinning domains is indicated by tilted white sticks, the periodicity along $a_{1,2}$ and c_0 is shown by vertical bars and the *c* axis of the monoclinic call by a white arrow).

In this image (Figure 9a), one also observes that the misfit structure is not strictly rigid but that the layers sometimes

Table 3. Physical Parameters of the Title Misfit Layered Materials

composition of misfit layered compounds	thermopower S (μV·K^{-1})	electrical resistivity r (W·cm)	thermal conductivity k (W·K^{-1}·cm^{-1})	temperature (K)	ZT
$[Ca_2(Co_{1.3}Cu_{0.7})O_4][CoO_2]_{1.59}$	+138	0.013	1.80	300	0.024
$[(Ca_{1.67}Y_{0.33})(Co_{0.97}Cu_{1.03})O_4][CoO_2]_{1.59}$	+150	0.131	1.17	300	0.004
$[(Ca_{1.73}Pr_{0.27})(Co_{1.03}Cu_{0.97})O_4][CoO_2]_{1.59}$	+145	0.022	1.34	300	0.021

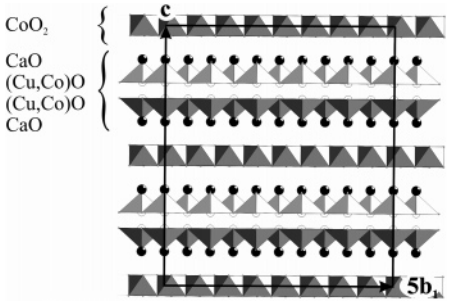

Figure 5. Projection along a of the approximant [$a \times 5b_1 \times c$] supercell, used for HREM image calculations.

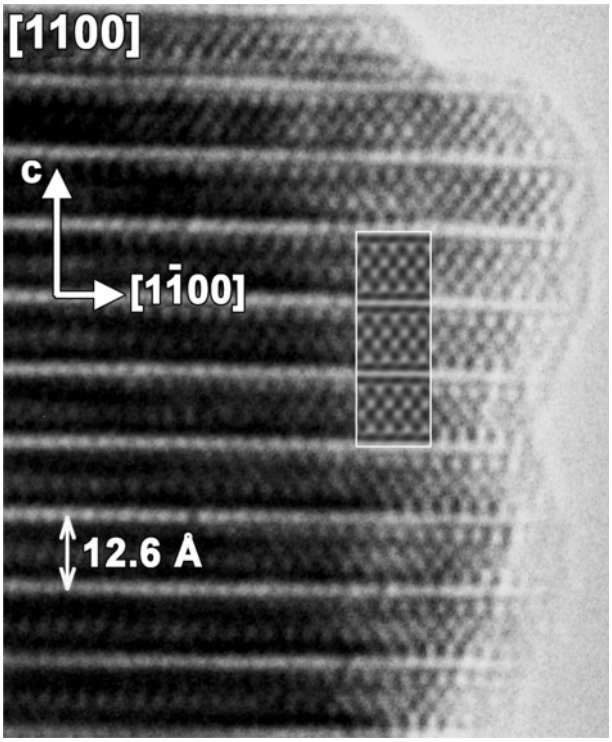

Figure 6. [1100] HREM image. The unit cell is indicated by a white outline, the simulated image is shown as an inset.

suffer curved shapes (similar to that indicated by a vertical row in Figure 7a). In the low part of the crystallite, the curvature is accommodated through the disappearance of one octahedron, since five CoO_6 octahedra are observed in upper $[CoO_2]_\infty$ layer for only four CoO_6 octahedra in the adjacent hexagonal layer (they are numbered 4 and 5 between the dark arrows). When extended, such a mechanism corresponds to a twinning by reticular pseudo-meriedry, as shown in Figure 9b. In the thick part of the crystallite, the twinning domains are 80° oriented, so that the twinning boundary is parallel to the $(101)_{NaCl}$ plane of the rock salt system. In the thinner part, the curvature of both types of layers allows accommodating the junction between the domains.

This TEM study shows the existence in misfit compounds of an incommensurate modulation at the level of the rock

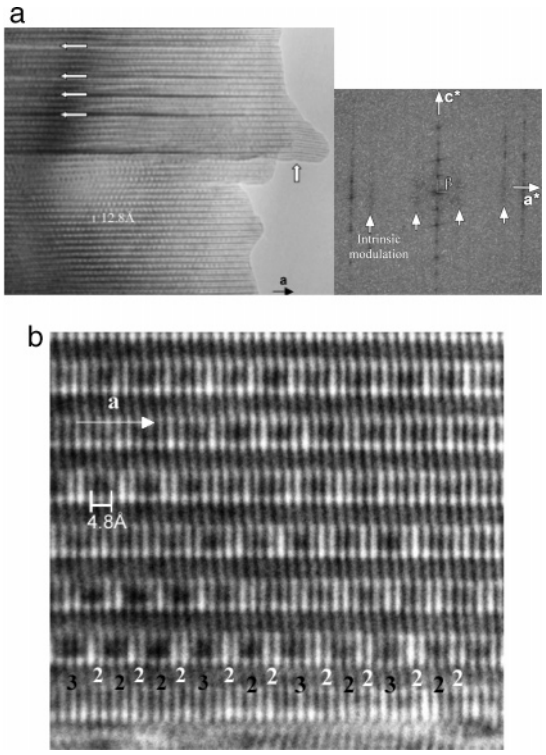

Figure 7. (a) [0100] overview image and FFT showing the specific contrast of the intrinsic modulation. The white arrows indicate extended defects. (b) Enlarged HREM image recorded in the thicker part.

salt layers, in the absence of lone pair stereoactivity of the cations, as well as the high flexibility of the complex structure through the different twinning mechanisms.

Transport Properties. The thermoelectric performance of a material is characterized by its power factor PF = S^2/ρ or its figure of merit $Z = S^2/(\rho\kappa)$, where S is the Seebeck coefficient, ρ is the resistivity, and κ is the thermal conductivity. For applications, thermoelectric materials should possess the largest Z. To evaluate the effect of Pr and Y on the thermoelectric performances of these misfits, the transport properties of the different $[Ca_{2-y}Ln_yCu_{0.7+y}Co_{1.3-y}][CoO_2]_{b_1/b_2}$ (Ln = Pr/Y) doped samples have been systematically measured. Figures 10 and 11 present the resistivity ρ and Seebeck S coefficients, respectively, as a function of temperature for the $[Ca_{2-y}Pr_yCu_{0.7+y}Co_{1.3-y}][CoO_2]_{b_1/b_2}$ and $[Ca_{2-y}Y_yCu_{0.7+y}Co_{1.3-y}][CoO_2]_{b_1/b_2}$ series. The thermal conductivity measured in $[Ca_{2-y}Pr_yCu_{0.7+y}Co_{1.3-y}][CoO_2]_{b_1/b_2}$ (y = 0.27) is presented in the inset of Figure 11. As the Pr content increases, ρ increases in the whole T range, especially at low T. However, the increase remains very small at RT (from 13 mΩ·cm for $y = 0$ to 19 mΩ·cm for $y = 0.27$) and will therefore not strongly reduce the Z factor. The thermal conductivity of $[Ca_{2-y}Pr_yCu_{0.7+y}Co_{1.3-y}][CoO_2]_{b_1/b_2}$ ($y = 0.27$) is small, close to 1.5 W·m^{-1}·K^{-1} at room temperature, a value typical of the results obtained in other polycrystalline misfits and in single crystals.[29] This small value is important

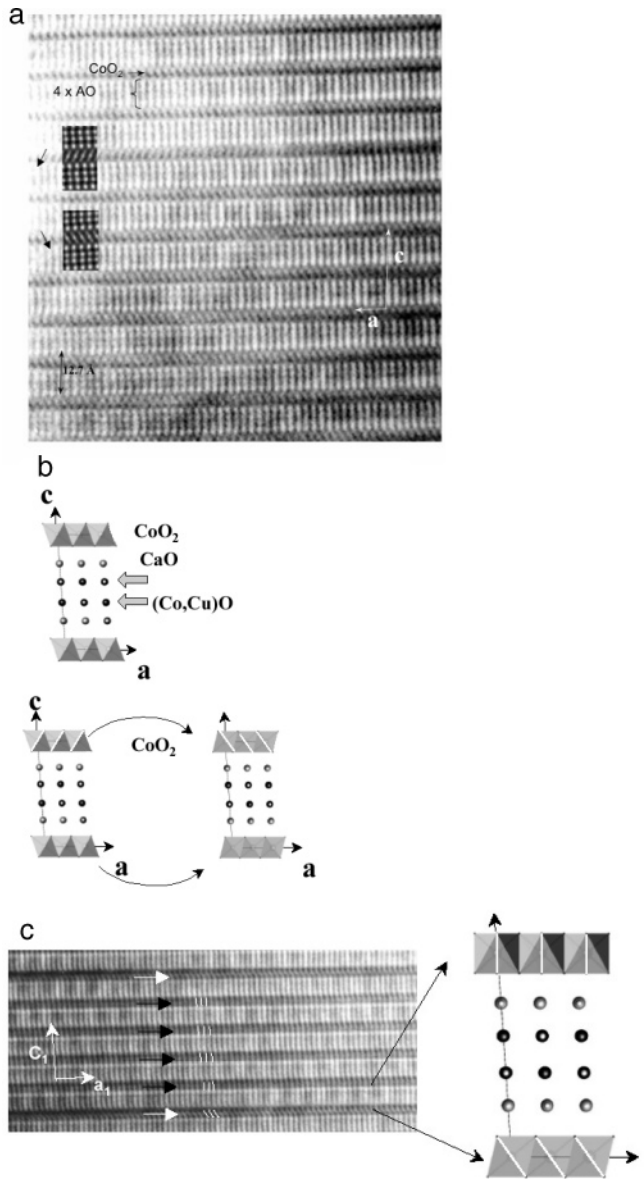

Figure 8. (a) Enlarged [0100] HREM image showing local 180° rotation of the hexagonal layer, (b) projection of the approximant model and model of rotation of one hexagonal layer, (c) enlarged [0100] HREM image showing local 120° rotation of the hexagonal layers and models. The calculated images are superimposed.

to maximize Z. The behavior at high T is changing from metallic ($d\rho/dT > 0$) for $y < 0.27$ to semiconducting ($d\rho/dT < 0$) for $y = 0.27$. This makes these samples interesting for high temperature applications as ρ will be smaller at higher T. Substituting Pr in the Ca/Co/Cu system induces an increase of the Seebeck coefficient: S changes from $+130\ \mu$V/K for $y = 0$ to $+145\ \mu$V/K for $y = 0.27$ at 300 K (Figure 11). The influence of the Pr substitution in Ca/Co/Cu can be 2-fold: first the Pr^{3+} for Ca^{2+} substitution can modify the cobalt valence, if we suppose a fixed oxygen content, and second the Pr^{3+} is magnetic ($4f^2$) and can therefore interact with the different Co sites (in the RS or in the CdI_2 layers). The results dealing with the substitution of Ca^{2+} by the nonmagnetic Y^{3+} ($4d^0$) can help clarify this issue.

The $\rho(T)$ and $S(T)$ data for the $[Ca_{1.67}Y_{0.33}Cu_{1.03}Co_{0.97}O_4]$-$[CoO_2]_{1.59}$ are presented (inset of Figure 10 and Figure 11). Concerning the resistivity data, the Y sample presents an insulating behavior in the whole T range as for the richest

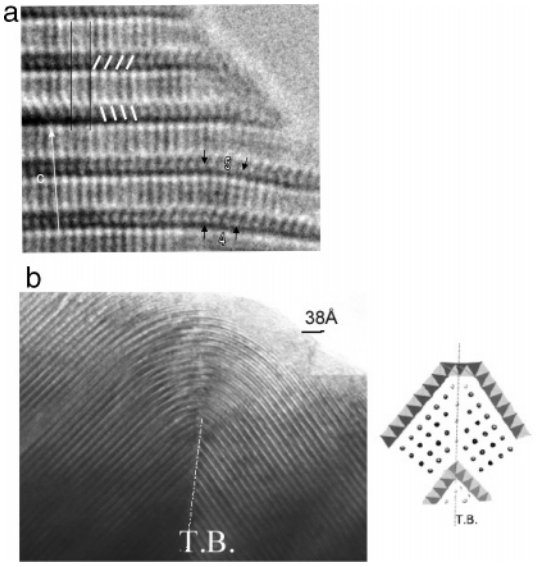

Figure 9. (a) Enlarged [0100] HREM image of an orthorhombic polytype built up from a chemical microtwinning and (b) overview of twinning domains resulting from reticular meriedry accommodated by the curvature of the two subsystems and schematical model of the $(101)_{NaCl}$ TB.

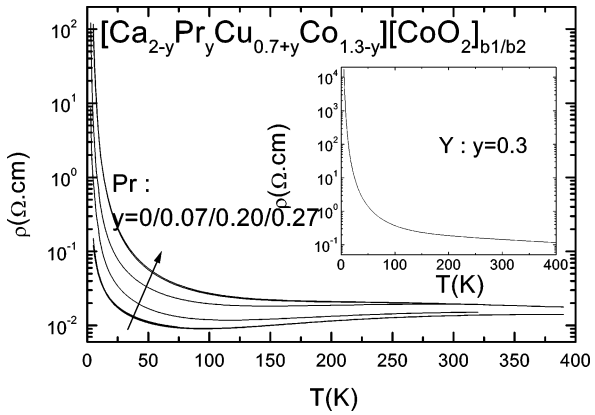

Figure 10. $\rho(T)$ of the Ca/Pr/Co/Cu series. Inset: $\rho(T)$ of Ca/Y/Co/Cu ($y = 0.3$).

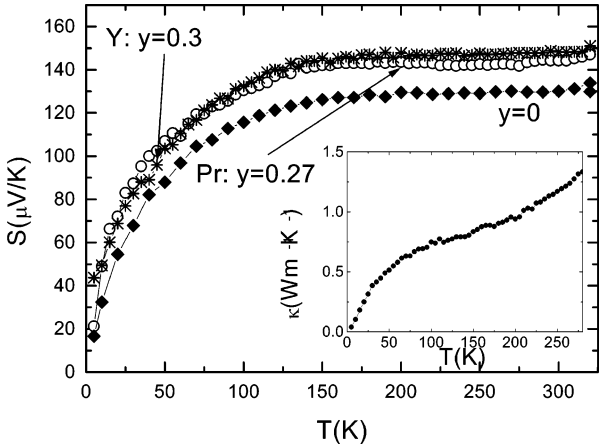

Figure 11. $S(T)$ of Ca/Co/Cu, Ca/Pr/Co/Cu ($y = 0.27$) and Ca/Y/Co/Cu ($y = 0.3$). Inset: $\kappa(T)$ of Ca/Pr/Co/Cu with $y = 0.27$.

Pr-doped samples, but it is much more resistive than the Pr compound, by 1 order of magnitude. Due to the polycrystalline nature of the sample, the possibility of an extrinsic contribution to the resistivity (grain boundaries effects) cannot be excluded. The Seebeck coefficient is not sensitive to this contribution and is therefore more interesting to

compare the effect of Y and Pr. Figure 11 shows that Y substitution is also very efficient to enhance the Seebeck coefficient: S at 300 K is close to $+150$ μV/K. Seebeck coefficients S of the Pr and Y samples are larger than the one of the Ca/Co/Cu compound in the whole T range, even down to 5 K. The increase of Seebeck coefficient can thus not be connected to a magnetic effect induced by Pr^{3+}, as Y^{3+} is nonmagnetic. This enhancement seems to be directly induced by a valence effect. Following ref 30, the Seebeck coefficient at high T depends on the ratio Co^{3+}/Co^{4+} in the CoO_2 layers and increases as the Co^{3+} concentration increases. Changing Ca^{2+} by Pr^{3+} or Y^{3+} corresponds to a decrease of the Co valence in the CoO_2 layer (i.e., an increase of the Co^{3+} content when x increases). This increase of the Co^{3+} content can explain the enhancement of the Seebeck coefficient at 300 K observed with Pr or Y substitution. A similar valence effect has been observed in $[Ca_2CoO_3][CoO_2]_{1.62}$ by tuning the oxygen content.[31]

Conclusions

The double substitution mechanism in the $[Ca_{2-y}Ln_y][Cu_{0.7+y}Co_{1.3-y}O_4][CoO_2]_{b_1/b_2}$ (Ln = Pr,Y) series stabilizes, for the first time, a misfit cobaltite with a **4S**-type lamellar structure, in which the two intermediate layers of the rock salt subsystem exhibit the same amount of copper and cobalt, namely, $[Ca_{1.73}Pr_{0.27}Cu_{0.97}Co_{1.03}O_4][CoO_2]_{1.61}$ and $[Ca_{1.67}Y_{0.33}Cu_{1.03}Co_{0.97}O_4][CoO_2]_{1.59}$. The interesting characteristic of these compounds is the presence of two modulations. One is associated to the misfit between the two structures whereas the second is intrinsic, associated to the only rock salt subsystem. The intrinsic modulation was determined from ED and HREM study. The latter presents similarities with those observed in the bismuth based cuprates and ferrites, where the $6s^2$ lone pair is considered as partly responsible of the modulation. In the title compounds, this factor can be ruled out. On the opposite, the similarity with the Sr-based ferrites $Sr_4Fe_6O_{13}$[23,24] is of interest since the intrinsic modulation is associated to the presence of additional oxygen in the intermediate rock salt layers, involving complex coordination of iron: trigonal bipyramids, tetragonal pyramids, and monocapped tetrahedra.[32] Unfortunately, our neutron diffraction does not allow the accurate modulated structure to be refined.

A significant increase of the thermopower is obtained by this double substitution in the Ca−Co−Cu−O system. The same effect is obtained by a magnetic or nonmagnetic cation, which shows that the enhancement is rather due to a valence effect than to a magnetic effect. By adding positive charges in the RS layer, the Co^{3+} concentration increases in the CoO_2 layers, and the Seebeck coefficient increases according to the modified Heikes formula.[30]

CM061163A

(27) Petricek, V.; Dusek, M. *JANA* 2000; Institute of Physics: Prague, Czech Republic, 2000.
(28) De Wolff, P. M. *Acta Crystallogr. A* **1974**, *30*, 777.
(29) Satake, A.; Tanaka, H.; Ohkawa, T.; Fujii, T.; Terasaki, I. *J. Appl. Phys.* **2004**, *96*, 931.
(30) Koshibae, W.; Tsutsui, K.; Maekawa, S. *Phys. Rev. B* **2000**, *62*, 6869.
(31) Karpinnen, M.; Fjellvag, H.; Konng, T.; Morita, Y.; Motohashi, T.; Yamauchi, H. *Chem. Mater.* **2004**, *16*, 2790.